Reservoir Computing Using On-Chip XGM-based Nonlinear Processing by Membrane SOAs on Si-MZI

Takuma Tsurugaya, Tatsurou Hiraki, *Member, IEEE*, Takuma Aihara, *Associate Member, IEEE*, Mitsumasa Nakajima, *Member, IEEE*, Nikolaos-Panteleimon Diamantopoulos, *Senior Member, IEEE*, Toru Segawa, *Member, IEEE*, and Shinji Matsuo, *Fellow, IEEE*

***Abstract*—We propose and demonstrate reservoir computing (RC) by all-optical nonlinear processing based on cross-gain modulation (XGM) in III-V membrane semiconductor optical amplifiers (SOAs) on a Si Mach-Zehnder interferometer (MZI). In the proposed configuration, two counter-propagating optical signals are input into the SOA-MZI from opposite ports, where they nonlinearly modulate each other via XGM, and are output to the other two ports. This realizes an on-chip XGM-based nonlinear processor that separately takes two input signals and returns two output signals, not requiring optical circulators. We implement an all-optical time-delay RC circuit using the SOA-MZI chip coupled with a fiber feedback loop. The strong optical confinement of membrane SOAs brings significant XGM, requiring only 47-mW power consumption of the SOA-MZI under -1-dBm average fiber input power. This low power consumption leads to an energy per nonlinear processing of only 11 pJ within the virtual node interval of 237 ps. Processing performances of the RC system are evaluated through information processing capacity (IPC) and the Santa-Fe time-series prediction task, which clearly indicates that the system has a significant nonlinear processing ability. Those dependencies on the optical power of the delayed feedback signal are investigated, clarifying that larger feedback power brings higher processing performances and stronger nonlinear transformation of the information. Our scheme offers a novel all-optical nonlinear functionality that is fully integratable onto Si-based photonic neural network chips.**

***Index Terms*—All-optical nonlinear processing, semiconductor optical amplifiers, reservoir computing, III-V/Si integration.**

I. INTRODUCTION

THE dramatic growth of artificial intelligence (AI) applications throughout society has aroused a large number of enthusiastic researches on photonic neural networks (PNNs) in recent years [1]–[13]. What makes photonics extraordinary for neuromorphic hardware is its inherent suitability for linear processing [4], [9], [11], the enlargement of the network scale for the time axis by low-loss optical waveguides [2], [3], [5]–[10], and the feasibility of high-density implementation by photonic integrated circuits (PICs), especially on the Si platform [4], [11]. Among the various PNN frameworks [11]–[13], reservoir computing (RC) [14], a class of recurrent neural networks (RNNs) with a fixed middle layer called the “reservoir,” is particularly promising in terms of implementation feasibility and low learning cost. Many studies on photonic RC have been conducted, demonstrating its applicability to computationally challenging problems despite its relatively simple implementation [1]–[10].

Aside from these encouraging viewpoints, one of the biggest challenges of PNNs is the implementation of nonlinear processing, which is essential for high-performance neural networks [15]–[17]. To fully exploit the potentials of PNNs, all-optical nonlinear processors are highly desired, as they free us from costly O/E/O conversions. One of the promising optical devices for this purpose is the semiconductor optical amplifier (SOA), which can exhibit significant saturable nonlinearity in the optical domain due to gain saturation [1], [2], [18], [19].

In this context, we recently proposed an all-optical nonlinear processing scheme based on cross-gain modulation (XGM) in a single SOA and demonstrated its successful application for time-delay RC using a membrane SOA on Si [10]. In the XGM-based scheme, two counter-propagating optical signals are input into a saturated SOA from opposite ports, and they nonlinearly modulate each other, executing two-variable nonlinear processing in the optical domain. Reflecting the strongly nonlinear nature of XGM, it enabled a significant nonlinear transformation of the input information, all-optically. From the implementation viewpoint, the counter-propagating feedback configuration effectively suppressed the unwanted lasing of the SOA, making the optical circuit "open" rather than a closed cavity. The counter-propagation also provided independence in the relative phase between the two optical signals, enabling phase-careless easy implementation even when using coherent light sources, or lasers.

However, despite these advantages, the potential of the XGM-based scheme was significantly limited due to the difficulty in on-chip integration; it necessitated two optical circulators (OCs) at the SOA's ports to separate the two input and two output signals into four individual waveguides (in

Manuscript received October 25, 2023; revised *** **, 202*; accepted *** **, 202*. Date of publication *** **, 202*; date of current version *** **, 202*. (*Corresponding author: Takuma Tsurugaya*.)

Takuma Tsurugaya, Tatsurou Hiraki, Takuma Aihara, Mitsumasa Nakajima, Nikolaos-Panteleimon Diamantopoulos, Toru Segawa, and Shinji Matsuo are with NTT Device Technology Labs, NTT Corporation, Atsugi 243-0198, Japan (e-mail: takuma.tsurugaya@ntt.com; tatsurou.hiraki@ntt.com; takuma.aihara@ntt.com; mitsumasa.nakajima@ntt.com; np.diamantopoulos@ntt.com; toru.segawa@ntt.com; shinji.matsuo@ntt.com).

Color versions of one or more of the figures in this article are available online at http://ieeexplore.ieee.org.

Digital Object Identifier 10.1109/JLT.2024.*******

[10], optical fibers). Since OCs are non-reciprocal devices requiring the Faraday effect, the necessity of OCs would strongly hinder on-chip integration of the XGM-based nonlinear processors. Dense integration of all-optical processors on a chip will be a key for high-performance PNNs. Therefore, a solution for the integration difficulty is essential for XGM-based nonlinear processing, which will explore its potentials and contribute to the advancement of PNNs.

To this end, we propose and demonstrate XGM-based nonlinear processing using two parallel SOAs integrated on a Si Mach-Zehnder interferometer (MZI), implemented on-chip without requiring OCs. The SOA-MZI configuration enables the separation of the counter-propagating input/output signals into four individual Si waveguides, thus serving as an on-chip two-input two-output nonlinear processor. The SOA-MZI consists of III-V membrane SOAs and phase shifters (PSs) integrated on both arms of a Si-MZI. Thanks to the advantages of membrane SOAs and PSs, the SOA-MZI consumes only 47 mW to exhibit significant XGM, showing high contrast ratios exceeding 20 dB. An average fiber input power of only -1 dBm was sufficient to induce significant XGM. The low power consumption results in an energy per nonlinear processing of only 11 pJ with a virtual node interval of 237 ps. We implement an all-optical time-delay RC circuit using the SOA-MZI chip coupled with a fiber feedback loop. In complement to our preliminary report [20] and to deepen the understanding, this study conducts a more systematic investigation of the RC system with additional measurements and analyses. The processing performances are evaluated through information processing capacity (IPC) and the Santa-Fe time-series prediction task, which clearly indicates that the XGM-based RC system possesses significant nonlinear processing ability. The dependence on the optical power of the delayed feedback signal is investigated, clarifying that a larger feedback power leads to higher processing performances and a stronger nonlinear transformation of the input information. The obtained results provide important insights into the relationship between the physical and computing aspects of XGM-based nonlinear processing.

II. Basic Concept and Device Configuration

Figure 1 illustrates the basic concept of the proposed XGM-based nonlinear processing and its device configuration. The configuration consists of III-V membrane SOAs and PSs integrated on both arms of a Si-MZI, constituting an SOA-MZI with inter-arm phase tunability. The Si-MZI consists of two 3-dB multi-mode interferometers (MMIs), and thus an input signal from one of the ports is evenly divided into both arms with equal power. Assuming balanced power levels in both arms and setting the MZI at the bar state, two counter-propagating input signals at the diagonal ports (P_{in}^{+} and P_{in}^{-}) are initially equally divided into both arms, then symmetrically induce XGM in both SOAs and are finally output to the rest bar ports (P_{out}^{+} and P_{out}^{-}) through interference in the MMIs. This means that the SOA-MZI has two input and two output ports that are spatially separated, while XGM between the two input signals occurs. As a result, this configuration exhibits the same functionality as that of the single SOA with two OCs [10], thus serving as an on-chip nonlinear processor. In the field of optical communication, such an MZI-based signal separation in XGM has been successfully utilized [21], [22].

In the computing aspect, this configuration can be regarded as an all-optical nonlinear processor that takes the two input intensity signals P_{in}^{+} and P_{in}^{-} and returns the two output intensity signals P_{out}^{+} and P_{out}^{-}. For easy understanding, let us first assume the static regime (i.e., neglect the transient response). In this case, the nonlinear processing would be simply described by a static function between the output $P_{\mathrm{out}}^{\pm}$ and the inputs $P_{\mathrm{in}}^{\pm}$, $P_{\mathrm{in}}^{\mp}$. The function would be primarily determined by the well-known saturable relation between $P_{\mathrm{out}}^{\pm}$ and $P_{\mathrm{in}}^{\pm}$ [1], [2], and additionally influenced by the oppositely propagating signal $P_{\mathrm{in}}^{\mp}$ via XGM. Due to the gain saturation mechanism of XGM, $P_{\mathrm{out}}^{\pm}$ would have a negative, saturable dependence on $P_{\mathrm{in}}^{\mp}$ [23], [24]. Consequently, the SOA-MZI would be described by a two-variable nonlinear function that directly calculates some nonlinear correlations between $P_{\mathrm{in}}^{\pm}$ and $P_{\mathrm{in}}^{\mp}$ through the gain saturation.

More realistically, when accounting for the transient responses of SOAs, the output signals are also influenced by the history of past input signals. This influence is due to the well-known pattern effect [25], [26]. Since the gain media or carriers in SOAs have finite response speeds (typically, ~10^{1}–10^{2} ps), they depend on the input history, and thus it is reflected to the current output signal. Therefore, the SOA-MZI can also exhibit a pattern-effect-induced dynamic nonlinearity in addition to the static nonlinearity. In a time-delay RC, such a dynamic response generates node-to-node connections due to the "inter-symbol crosstalk," which is believed to improve processing performance by enriching the diversity of node states [7], [27], [28]. Figure 2(a) shows an optical microscope image of a fabricated SOA-MZI, where III-V membrane SOAs and PSs are heterogeneously integrated on a Si-MZI [29], [30]. Cross-sectional scanning electron microscope (SEM) images of a PS and an SOA are shown in Figs. 2(b) and 2(c), respectively, and Figs. 2(d) and 2(e) illustrate those corresponding schematics. The PS consists of a 500-μm-long InGaAsP bulk core for reverse-bias phase tuning, while the SOA consists of a 300-μm-long InGaAsP-based multiple quantum well (MQW) core optically coupled to a buried Si core. This heterogeneous integration involving different buried heterostructures (BHs) is enabled by our III-V/Si integration technology with a regrowth technique. A more detailed description of the device can be found in [29], [30].

To verify the concept of on-chip signal separation, we initially checked the input-output characteristics of the SOA-MZI chip itself for both propagation directions. Figures 3(a) and 3(b) schematically illustrate the measurement setups for the forward and backward directions, respectively. Each Si waveguide is connected to an SiO_x-based spot-size converter

(SSC), facilitating low-loss coupling with a high-numerical-aperture (HNA) fiber at the chip facet. As illustrated, we coupled HNA fibers to all four ports to enable simultaneous measurement of both the bar and cross outputs, using 2-channel HNA fiber arrays for the left and right facets. For the inter-arm power-level balancing, we set the injection current of SOA1 and SOA2 (I_{SOA1} and I_{SOA2}) at the same value of 15 mA. The small injection current of 15 mA was expected to be sufficient for the membrane SOAs to have on-chip gain, thanks to the small active volume with strong optical confinement [10], [29]. We then fine-tuned the inter-arm relative phase by adjusting the bias voltages of PS1 and PS2 to set the SOA-MZI at either the bar or cross states. We chose to use the bar state, although the cross state would also have been viable.

In this arrangement, we input a continuous-wave (CW) light from a tunable laser diode (TLD, Santec TSL-550) into the lower-left (Fig. 3(a), forward) or upper-right (Fig. 3(b), backward) port and simultaneously measured both the bar and cross outputs to evaluate the contrast ratios. The wavelength of the input light was set at 1530 nm, and its fiber power P_{in} was -2 dBm. Since we chose to use the bar state, the bar output was regarded as a desired output while the cross output as an unintended crosstalk. Figures 3(c) and 3(d) show the fiber output powers at the bar and cross ports (P_{bar} and P_{cross}) measured for the forward and backward setups, respectively, where V_{PS2} was fixed at 2.25 V and V_{PS1} was swept. For both directions, the interference curves were clearly observed, and the contrast ratios exceeded 20 dB at $V_{\mathrm{PS1}} = 1$ V. These large contrast ratios indicate that the power levels of both arms were well balanced and the inter-arm phase was well tuned to π/2, successfully achieving the bar state. Note that P_{bar} was -1.8 dBm and 1.1 dBm at $V_{\mathrm{PS1}} = 1$ V for the forward and backward setups, respectively, meaning that a fiber-to-fiber lossless state was achieved. Therefore, in the following experiments, we fixed the bias point of the SOA-MZI at $I_{\mathrm{SOA1}} = I_{\mathrm{SOA2}} = 15$ mA, $V_{\mathrm{PS1}} = 1$ V, $V_{\mathrm{PS2}} = 2.25$ V. P_{bar} in the forward case being smaller than that in the backward case should be because of a lower SSC/fiber coupling efficiency in the lower-right port due to some fiber alignment error; since we used a 2-channel HNA fiber array with a fixed fiber-to-fiber pitch, simultaneous perfect alignment of both of the bar and cross ports was not achieved, resulting in the larger coupling loss in the lower-right port. Here, the total power consumption of the SOA-MZI at this bias point was as low as 47 mW, thanks to the small injection current required for the SOAs and the reverse-bias operation of the PSs [10], [29], [30].

Then, we also measured the static input-output power characteristic of the bar port at this bias point for each propagation direction, in order to check nonlinearity of the SOA-MZI and its power scale. Figures 3(e) and 3(f) show the measurement results, where significant gain-saturation nonlinearity is clearly observed for the input power range over -2 dBm for both directions. For the lower input power range, the nonlinearity in the forward direction is weaker than that in the backward direction, which reasonably reflects the difference in the net input power into the SOAs between both directions; for the forward case, the input light first propagates through the PSs with some optical losses, which results in the smaller input power into the SOAs and thus the weaker nonlinearity.

III. Implementation of XGM-based RC

Using the SOA-MZI chip and a fiber feedback loop, we implemented an XGM-based time-delay RC system as shown in Fig. 4(a). A masked input signal $m_i u(n)$ from an arbitrary waveform generator (AWG, Keysight M8195A) with 8-bit resolution is applied to an external Mach-Zehnder modulator (MZM, SHF 46210C) to intensity-modulate the CW light from the TLD set at 1530 nm. To linearly modulate the optical intensity, we set the bias point of MZM near the quadrature point and set V_{pp} (i.e., maximum swing voltage) to be smaller than V_π, making the RF component of the optical input signal almost identical to $m_i u(n)$ itself. $n = 1,2,\cdots,L$ denotes the time-step index of time-series input signal $u(n)$ with data length of L. $i = 1,2,\cdots,N$ denotes the node index of the mask function m_i with a node number of N. In this study, we set $N = 200$ and let m_i take arbitrary random values ranging from -1 to 1. The optical input signal was input into the SOA-MZI chip from the lower-left port. Then, the output signal from the lower-right bar port, which was regarded as the reservoir response $x_i(n)$, was guided into a single-mode fiber. 10% of the output signals was tapped by a 10-dB optical coupler and measured as the reservoir response through an erbium-doped fiber amplifier (EDFA, Alnair Labs LNA-220-C), an optical bandpass filter (BPF, Santec OTF-920), a photodiode with a trans-impedance amplifier (PD/TIA, Hewlett-Packard 11982A), and a digital storage oscilloscope (DSO, Keysight DSO-Z 634A). The remaining 90% was for a fiber delay line. The fiber delay line included a polarization controller and a variable optical attenuator (VOA), and the total length was ~10 m. Using the VOA, we controlled the attenuation of the feedback power, α_{FB} (dB). The delayed signal was fed-back to the SOA-MZI chip from the upper-right port, was equally divided into both arms, and induced symmetrical XGM with the input signal in the two SOAs. Finally, the feedback signal was output to the upper-left port due to the bar state operation and was removed from the RC circuit. The counter-propagating configuration brought the advantages of relative-phase independence and suppression of SOA lasing, which were practically important for successful RC implementation.

The removed feedback signal was guided to an optical spectrum analyzer to monitor its spectrum and check the stability of the RC circuit. Through this monitoring, we confirmed that the RC circuit operated stably without lasing down to an attenuation of 2 dB. When we set the attenuation to 0 dB, the spectrum exhibited a lasing peak, meaning that some cavity including the SOAs was formed and reached its lasing threshold. Ideally, this RC circuit would be open and thus free from cavity formation. However, in reality, there should have existed some finite reflections at waveguide interfaces both outside and inside the SOA-MZI chip, such as

the SSC/fiber facets or the buried active core/InP waveguide interfaces of the SOAs and PSs. Such finite reflections should have formed an unintended cavity including the SOAs and the fiber delay line. Therefore, we limited the minimum attenuation to 2 dB for the stable operation of the SOAs with lasing suppression. As long as the lasing is suppressed (i.e., the gain is not clamped), the SOAs exhibit the desired gain-saturation nonlinear behavior even with such finite reflections, which should ensure successful operation of the XGM-based nonlinear processing.

We set the time interval of one node as $\theta = \tau/(N+1)$, where τ is the round-trip delay time of the feedback circuit, as precisely measured by the impulse response measurements shown in the following. This setting established the connections between adjacent nodes, resulting in the ring-shaped recurrent network as shown in Fig. 4(b). Then, the output signal was obtained by taking the linear combination of each node's response: $o(n) = w_1 x_1(n) + \cdots + w_N x_N(n)$, which was performed offline on a personal computer. As is evident from Figs. 4(a) and 4(b), XGM in the SOA-MZI plays an essential role in this RC system; it is responsible for both the nonlinear transformation and recurrence of the input information. Therefore, the performances of this RC system should strongly reflect the computational characteristics of XGM.

Before the RC performance evaluation, we measured the impulse responses of this RC system to characterize its basic behavior. The baseline optical input power at the fiber was set to -1 dBm expecting a significant nonlinearity, and a positive input pulse was generated through the MZM with an amplitude of $V_{pp}/2$ and pulse duration of 1 ns. Figure 5 shows the impulse responses measured under the feedback attenuations of (a) full cutoff, (b) 10 dB, (c) 4 dB, and (d) 2 dB. While there was not an apparent response in the full cutoff and 10-dB cases, the 4-dB case clearly exhibited a negative-polarity response pulse at t = 47.7 ns, which corresponded to the round-trip delay time τ expected from the fiber length of ~10 m. This polarity-inverted response is a distinctive feature of XGM. The 2-dB case exhibited a more significant response; after the negative response at $t = \tau$, a clear positive response appeared at $t = 2\tau$, and again a negative response appeared at $t = 3\tau$. This periodic polarity inversion is clear proof that the response of this RC system was based on XGM.

We would like to emphasize that such significant XGM was achieved with a small injection current for the SOAs: $I_{\mathrm{SOA1}} = I_{\mathrm{SOA2}} = 15$ mA and the average fiber input power of only -1 dBm at the lower-left port. This injection current is very small compared with those of conventional SOAs utilized as nonlinear processors in PNNs, which typically range from ~100 mA to ~300 mA [2], [18], [19]. As demonstrated and discussed in our former study with a single membrane SOA [10], this low-power-consumption, low-power-scale nonlinearity is enabled by the membrane SOA's feature of a small active area with strong optical confinement.

We also comment on how the unintended crosstalk into the upper-right port influences the behavior of this RC circuit. Let us denote the forward optical signal in each arm just before the right-side MMI as P^{+}_{arm1} and P^{+}_{arm2}. In accordance with the good interference characteristics (Figs. 3(c) and 3(d)), the finite contrast ratio is considered mainly due to the power imbalance between the two arms: $P^{+}_{\mathrm{arm1}}/P^{+}_{\mathrm{arm2}} \neq 1$. Here, the fiber delay line combined with the right-side MMI forms a loop mirror, where the intended reservoir response (anti-clockwise) and the unintended crosstalk (clockwise) interfere via the MMI. Therefore, owing to the loop-mirror mechanism, the power splitting ratio of the delayed feedback signals into both arms (P^{-}_{arm1} and P^{-}_{arm2}) becomes the same as that of the forward signals: $P^{-}_{\mathrm{arm1}}/P^{-}_{\mathrm{arm2}} = P^{+}_{\mathrm{arm1}}/P^{+}_{\mathrm{arm2}}$ (under the assumption of an ideal 3-dB MMI characteristic and inter-arm phase of $\pi/2$). This means that the crosstalk induces more gain consumption in the arm with originally larger power due to stronger feedback into it, which results in the mitigation of the power imbalance. Therefore, the crosstalk should not cause a problem but rather brings a self-correction effect of the power imbalance, which should stabilize the SOA-MZI's operation as the two-input two-output nonlinear processor.

IV. RC Performance Evaluation

In the following performance evaluation, we once again set the TLD wavelength to 1530 nm and maintained the baseline optical input power at the fiber at -1 dBm. The round-trip delay time τ of 47.7 ns and the node number N of 200 yielded the node interval θ of 237 ps. This node interval was comparable with the time scale of the SOAs' transient response, as observed in Fig. 5. Therefore, the reservoir response should have been influenced by both the static and dynamic nonlinearities of the SOAs. We set the DSO's sampling rate to 20 GSa/s, resulting in ~4.7 sampling points per node. We took an average of these sampling points to obtain a reservoir response of each node, expecting that both the static and dynamic nonlinearities would be reflected.

Figure 6 is an example of the raw experimental data of the performance evaluation for 2-dB attenuation, showing the input voltage signal itself from the AWG and the corresponding reservoir response signal. The baseline ($t < 0$) corresponds to the zero levels of the signals. The plotted time range is the beginning of the signal measurement, where the time-step index n = 1. While there is a similarity in the waveform between the input and reservoir response, the latter appears significantly distorted compared with the former. This distortion should reflect both the static and dynamic nonlinearities of the SOAs.

For a systematic investigation, we conducted performance evaluation measurements across various feedback attenuations: 2 dB, 4 dB, 6 dB, 10 dB, 20 dB, and full cutoff. For each attenuation point, we repeated the same measurements three times to check the reproducibility and to systematically investigate the dependence on feedback power.

A. Information Processing Capacity

We first measured and evaluated the IPC [31] of the RC system. IPC was originally introduced in [31] as a task-independent measure of RC's processing performance and is widely adopted for various RC studies [6]–[8], [10]. In the

evaluation, the input signal $u(n)$ ($n = 1, \cdots, L$) is set to a random sequence taking arbitrary values from -1 to 1, and the corresponding reservoir responses $x_i(n)$ are measured. Then, the target signal $y(n)$ to reproduce is set to

$$y(n) = \prod_j P_{d_j}\left(u(n - k_j)\right) \tag{1}$$

, where j is the index of the factors in the product, d_j is the polynomial degree, k_j is the delay step towards the past, and P_{d_j} is the Legendre polynomial function with the degree of d_j. Since (1) consists of the polynomial transformations of the past input values, we can evaluate the nonlinearly-transformed memory of the RC system for the given set of polynomial degrees $\{d_1, d_2, \cdots\}$, by calculating how well the system can reproduce (1). The reproducibility is called "capacity" and is given by [31]:

$$C = \frac{\boldsymbol{y}^T X (X^T X)^{-1} X^T \boldsymbol{y}}{\|\boldsymbol{y}\|^2} \tag{2}$$

, where $\boldsymbol{y} = [y(1), y(2), \cdots, y(L)]$ is the vectorized target signal sequence, and $X \equiv [x_{ni}]_{L\times N} = [x_i(n)]_{L\times N}$ is the $L \times N$ matrix consisting of the reservoir response $x_i(n)$. For a given total polynomial degree of D, the calculation of C is performed for every possible set of $\{k_1, k_2, \cdots\}$ and $\{d_1, d_2, \cdots\}$ under $d_1 + d_2 + \cdots = D$ is satisfied. Then, by summing the values of C for every possible set, we obtain the D-th order memory capacity (MC), MC^D. MC^1 denotes the linear MC, while MC^D for $D \geq 2$ denotes the nonlinear MCs. Summation of the MCs for D, $\mathrm{MC}^1 + \mathrm{MC}^2 + \cdots$, is the total memory capacity (TMC), which evaluates the total memory of the RC system.

We set the data length L to 2,000. Corresponding to this finite data length, we set the "cutoff capacity" C_{CO} (i.e., if $C < C_{\mathrm{CO}}$, then C is assumed to be zero [7], [10]) to 0.15, which was high enough to eliminate the contribution of pseudo memory originating from the finite statistics [31]. We evaluated the MCs for the orders ranging from $D = 1$ to $D = 5$ and thus calculated the TMC by $\mathrm{MC}^1 + \cdots + \mathrm{MC}^5$.

Figure 7 shows a representative example of the IPC that recorded the highest TMC among the three-time measurements for each attenuation point. First, it is evident that the TMC increases as the feedback attenuation decreases. This can be reasonably attributed to the strength of XGM; when the feedback power is larger, the delayed feedback signal more strongly modulates the input signal via XGM, and then its information is more significantly reflected in the next time step, resulting in the larger TMC. It is consistent with the impulse responses in Fig. 5, where larger feedback power resulted in a longer response-pulse-train lifetime. Second, it is also evident that the RC system is highly nonlinear; the majority of TMC is composed of nonlinear MCs, and there are significant contributions of high-order MCs like MC^3, MC^4, and MC^5. Note that even in the case of no feedback, there are very few but finite MCs up to $D = 3$. These residual MCs are considered to stem from the finite response speeds of the components in the RC system such as the AWG, DSO, or SOA itself, and should be regarded as some offset not associated with XGM. In addition, note that the high-order MCs, MC^4 and MC^5, appear only under feedback, indicating that they are purely associated with the occurrence of XGM. Therefore, Fig. 7 represents the significant nonlinear processing ability of XGM.

B. Santa-Fe Time-series Prediction

Next, we measured and evaluated the performance on the Santa-Fe time-series prediction task, which is a nonlinear benchmark task commonly adopted for RC studies [3], [5], [6], [9], [16]. In this task, the input signal $u(n)$ is set to the discrete time-series data of a laser output in a chaotic oscillation state. Then, the target signal $y(n)$ to predict is set to the one-step-ahead shifted version of the input itself: $y(n) = u(n + 1)$. It is believed that this task requires significant nonlinearity for high-accuracy prediction [6], [16]. The time-series data comprised 4,000 points in total. We used 3,000 points for training (i.e., learning the output weights) and the remaining 1,000 for testing (i.e., evaluating the prediction performance). The output signal was given by $o(n) = w_1 x_1(n) + \cdots + w_N x_N(n)$, and learning of the output weights $w_1, \cdots, w_N$ was executed by the ridge regression method. The prediction performance was then evaluated in terms of normalized mean-square error (NMSE):

$$\mathrm{NMSE} = \frac{\langle (y - o)^2 \rangle_L}{\langle (y - \langle y \rangle_L)^2 \rangle_L} \tag{3}$$

, where $\langle y \rangle_L$ denotes the time average of $y(n)$ over $n = 1$ to L, with L being 1,000 in this case.

Figure 8 shows a representative example of the testing results that recorded the lowest NMSE among the three-time measurements for each attenuation point: (a) full cutoff, (b) 20 dB, (c) 10 dB, (d) 6 dB, (e) 4 dB, and (f) 2 dB. The difference between the cases of no feedback (a) and large feedback (e,f) is evident; the prediction accuracy is very poor in the former, while high-accuracy prediction is obtained in the latter. This indicates that optical feedback is essential for the RC system to solve the Santa-Fe task. The lowest NMSE value was obtained at an attenuation point of 4 dB, and it was as low as 0.104. This value is comparable to those by other experimental photonic RC systems: NMSE = 0.124 in [3], 0.146 in [5], and 0.06 in [9], and is almost the same as that by our single-SOA XGM-based RC: NMSE = 0.112 in [10]. Therefore, this RC system has a good performance on the Santa-Fe task. Accordingly, together with the aforementioned IPC evaluation, the result here clearly demonstrates a significant nonlinear processing ability of our RC system. In the aspect of energy consumption for nonlinear processing, the SOA-MZI can be regarded as a nonlinear processor with the power consumption $P_{\mathrm{SOA-MZI}}$ of 47 mW, and its energy per nonlinear processing E_{NL} is given by

$$E_{\mathrm{NL}} = \frac{P_{\mathrm{SOA-MZI}}}{1/\theta}. \tag{4}$$

The denominator $1/\theta$ expresses the nonlinear processing rate and was 4.2 GHz for the adopted θ of 237 ps. Accordingly, we obtained a low E_{NL} of only 11 pJ, thanks to the low-power-consumption advantages of our membrane SOAs and PSs. For comparison, if we were to use conventional SOAs, which would require injection current of a few hundreds of mA (e.g., 187 mA in [2], 240 mA and 280 mA in [18]) for significant nonlinearity, they would consume a few hundreds of mW per a single SOA. Thus, under the same nonlinear processing rate of 4.2 GHz, they

would give E_{NL} of several tens of pJ or even higher, which highlights the low nonlinear processing energy of our processor.

C. Feedback Power Dependence and Discussion

For a more systematic analysis and discussion, we statistically evaluate the performances on the basis of the data sets of three-time measurements; in Fig. 9, the TMC and NMSE values are averaged over the three data points, and the error bars are defined by the maximum and minimum values among the three. As for the TMC, the error bars are relatively small, confirming clearly that larger feedback power brings a higher TMC. As previously described, this trend can be explained by the strength of XGM. On the other hand, the NMSE on the Santa-Fe task exhibits relatively large error bars, making it difficult to distinguish the performance differences between adjacent attenuation points, especially those between 2 dB and 4 dB. The relatively large error bars indicate that the RC system had some fluctuation, and the Santa-Fe task sensitively reacted to it. One of the likely origins of such fluctuation is the fiber-induced instability of polarization, which would be removed by implementing the delay line on-chip by use of low-loss waveguides [9], [32], instead of fibers. Nonetheless, the solid-line trace of the averaged NMSE values most likely indicates a trend that larger feedback power brings higher performance on this task.

Finally, we evaluated the nonlinearity strength on the basis of the IPC data. Since the IPC is composed of MCs with different polynomial degrees, the ratio of each MC to the TMC specifies what kinds of nonlinearities the RC system has. For such an analysis, we calculated the normalized MCs: $\mathrm{MC}^D/\mathrm{TMC}$ for each data point and averaged them over the three measurement points for each degree D. In Fig. 10, the averaged normalized MCs are plotted in the same manner as Fig. 7. The error bar is also plotted for each MC component, which is defined by the maximum and minimum values among the three. Since the error bars are relatively small, the averaged values should well represent the computing characteristics. They clearly indicate a trend that the larger the feedback power, the stronger the nonlinearity. This can be reasonably associated with a physical picture that the larger feedback power induces stronger gain saturation [23]–[26] and thus brings enhanced nonlinearity. The significant contribution of the high-order nonlinearities is also remarkable. For example, at 2 dB, the MCs with $D \geq 3$ account for over 50% of the TMC. This highlights XGM's ability to induce strong nonlinear transformation of the information in the optical domain.

Accordingly, the results in Figs. 9 and 10 can be summarized to a key consequence: larger feedback power induces stronger XGM, which brings more memory, stronger nonlinearity, and higher processing performance. This reveals the relationship between the physical and computing aspects of the XGM-based nonlinear processing and gives us a guide for the effective utilization of this processing scheme for PNNs.

V. Conclusion

We have proposed and demonstrated XGM-based nonlinear processing that can be implemented on-chip by the SOA-MZI configuration. The on-chip implementation feasibility and low-power-consumption advantage will be of particular importance for its application to densely integrated PNNs. Since the SOA-MZI is achieved by our membrane III-V/Si platform, it will be compatible with other essential PNN components such as laser-diode light sources [33], [34] or Si-based compact linear processors [4], [11].

The computing characteristics of the XGM-based RC system have been systematically investigated. Its ability to induce strong nonlinear transformation of the information has been clarified. The investigation has also revealed the physically reasonable consequence that stronger feedback power brings more memory and stronger nonlinear transformation. The unique computing functionality of our scheme will explore the potentials of all-optical nonlinear processing and advance the development of Si-based PNNs.

References

[1] K. Vandoorne, J. Dambre, D. Verstraeten, B. Schrauwen, and P. Bienstman, "Parallel Reservoir Computing Using Optical Amplifiers," *IEEE Transactions on Neural Networks*, vol. 22, no. 9, pp. 1469–1481, Sep. 2011, doi: 10.1109/TNN.2011.2161771.

[2] F. Duport, B. Schneider, A. Smerieri, M. Haelterman, and S. Massar, "All-optical reservoir computing," *Opt. Express, OE*, vol. 20, no. 20, pp. 22783–22795, Sep. 2012, doi: 10.1364/OE.20.022783.

[3] L. Larger *et al*., "Photonic information processing beyond Turing: an optoelectronic implementation of reservoir computing," *Opt. Express, OE*, vol. 20, no. 3, pp. 3241–3249, Jan. 2012, doi: 10.1364/OE.20.003241.

[4] K. Vandoorne *et al*., "Experimental demonstration of reservoir computing on a silicon photonics chip," *Nat Commun*, vol. 5, no. 1, p. 3541, Mar. 2014, doi: 10.1038/ncomms4541.

[5] Y. Kuriki, J. Nakayama, K. Takano, and A. Uchida, "Impact of input mask signals on delay-based photonic reservoir computing with semiconductor lasers," *Opt. Express, OE*, vol. 26, no. 5, pp. 5777–5788, Mar. 2018, doi: 10.1364/OE.26.005777.

[6] J. Pauwels, G. Verschaffelt, S. Massar, and G. Van der Sande, "Distributed Kerr Non-linearity in a Coherent All-Optical Fiber-Ring Reservoir Computer," *Front. Phys.*, vol. 0, 2019, doi: 10.3389/fphy.2019.00138.

[7] K. Harkhoe and G. Van der Sande, "Task-Independent Computational Abilities of Semiconductor Lasers with Delayed Optical Feedback for Reservoir Computing," *Photonics*, vol. 6, no. 4, Art. no. 4, Dec. 2019, doi: 10.3390/photonics6040124.

[8] F. Köster, S. Yanchuk, and K. Lüdge, "Insight into delay based reservoir computing via eigenvalue analysis," *J. Phys. Photonics*, vol. 3, no. 2, p. 024011, Apr. 2021, doi: 10.1088/2515-7647/abf237.

[9] M. Nakajima, K. Tanaka, and T. Hashimoto, "Scalable reservoir computing on coherent linear photonic processor," *Commun Phys*, vol. 4, no. 1, pp. 1–12, Feb. 2021, doi: 10.1038/s42005-021-00519-1.

[10] T. Tsurugaya *et al*., "Cross-gain modulation-based photonic reservoir computing using low-power-consumption membrane SOA on Si," *Opt. Express, OE*, vol. 30, no. 13, pp. 22871–22884, Jun. 2022, doi: 10.1364/OE.458264.

[11] Y. Shen *et al*., "Deep learning with coherent nanophotonic circuits," *Nature Photon*, vol. 11, no. 7, pp. 441–446, Jul. 2017, doi: 10.1038/nphoton.2017.93.

[12] J. Feldmann, N. Youngblood, C. D. Wright, H. Bhaskaran, and W. H. P. Pernice, "All-optical spiking neurosynaptic networks with self-learning capabilities," *Nature*, vol. 569, no. 7755, pp. 208–214, May 2019, doi: 10.1038/s41586-019-1157-8.

[13] M. Nakajima, K. Inoue, K. Tanaka, Y. Kuniyoshi, T. Hashimoto, and K. Nakajima, "Physical deep learning with biologically inspired training method: gradient-free approach for physical hardware," *Nat Commun*, vol. 13, no. 1, Art. no. 1, Dec. 2022, doi: 10.1038/s41467-022-35216-2.

[14] G. Tanaka *et al*., "Recent advances in physical reservoir computing: A review," *Neural Networks*, vol. 115, pp. 100–123, Jul. 2019, doi: 10.1016/j.neunet.2019.03.005.

[15] A. Goudarzi, A. Shabani, and D. Stefanovic, "Exploring transfer function nonlinearity in echo state networks," in *2015 IEEE Symposium on Computational Intelligence for Security and Defense Applications (CISDA)*, May 2015, pp. 1–8. doi: 10.1109/CISDA.2015.7208637.

[16] M. Inubushi and K. Yoshimura, "Reservoir Computing Beyond Memory-Nonlinearity Trade-off," *Sci Rep*, vol. 7, no. 1, p. 10199, Aug. 2017, doi: 10.1038/s41598-017-10257-6.

[17] C. Nwankpa, W. Ijomah, A. Gachagan, and S. Marshall, "Activation Functions: Comparison of trends in Practice and Research for Deep Learning," *arXiv:1811.03378 [cs]*, Nov. 2018, Accessed: Sep. 28, 2021. [Online]. Available: http://arxiv.org/abs/1811.03378

[18] G. Mourgias-Alexandris, A. Tsakyridis, N. Passalis, A. Tefas, K. Vyrsokinos, and N. Pleros, "An all-optical neuron with sigmoid activation function," *Opt. Express, OE*, vol. 27, no. 7, pp. 9620–9630, Apr. 2019, doi: 10.1364/OE.27.009620.

[19] B. Shi, K. Prifti, E. Magalhães, N. Calabretta, and R. Stabile, "Lossless Monolithically Integrated Photonic InP Neuron for All-Optical Computation," in *Optical Fiber Communication Conference (OFC) 2020 (2020), paper W2A.12*, Optica Publishing Group, Mar. 2020, p. W2A.12. doi: 10.1364/OFC.2020.W2A.12.

[20] T. Tsurugaya *et al.*, "Cross-Gain Modulation-Based Reservoir Computing Using Membrane SOAs on Si-MZI," in *Conference on Lasers and Electro-Optics (2022), paper SS1D.2*, Optica Publishing Group, May 2022, p. SS1D.2. doi: 10.1364/CLEO_SI.2022.SS1D.2.

[21] Y. Shibata *et al.*, "Monolithically Integrated Parallel-Amplifier Structure for Filter-Free Wavelength Conversion," *Jpn. J. Appl. Phys.*, vol. 41, no. 2S, p. 1194, Feb. 2002, doi: 10.1143/JJAP.41.1194.

[22] T. Segawa *et al.*, "All-optical wavelength-routing switch with monolithically integrated filter-free tunable wavelength converters and an AWG," *Opt. Express, OE*, vol. 18, no. 5, pp. 4340–4345, Mar. 2010, doi: 10.1364/OE.18.004340.

[23] H. Takeda and H. Uenohara, "Novel Optical Signal Regeneration System Using Cascaded Wavelength Converter Based on Cross-Gain Modulation in Semiconductor Optical Amplifiers," *Jpn. J. Appl. Phys.*, vol. 42, no. 12A, p. L1446, Nov. 2003, doi: 10.1143/JJAP.42.L1446.

[24] G. Contestabile, "Wavelength Conversion of PAM signals by XGM in SOAs," in *Asia Communications and Photonics Conference 2016 (2016), paper AF4H.4*, Optica Publishing Group, Nov. 2016, p. AF4H.4. doi: 10.1364/ACPC.2016.AF4H.4.

[25] J. Annetts, M. Asghari, and I. H. White, "The effect of carrier transport on the dynamic performance of gain-saturation wavelength conversion in MQW semiconductor optical amplifiers," *IEEE Journal of Selected Topics in Quantum Electronics*, vol. 3, no. 2, pp. 320–329, Apr. 1997, doi: 10.1109/2944.605674.

[26] R. Matsumoto, G. Contestabile, Y. Yoshida, A. Maruta, and K. Kitayama, "Pattern-independent wavelength conversion of PAM signals in SOAs," in *2016 21st OptoElectronics and Communications Conference (OECC) held jointly with 2016 International Conference on Photonics in Switching (PS)*, Jul. 2016, pp. 1–3.

[27] L. Appeltant *et al.*, "Information processing using a single dynamical node as complex system," *Nat Commun*, vol. 2, no. 1, p. 468, Sep. 2011, doi: 10.1038/ncomms1476.

[28] L. Appeltant, G. Van der Sande, J. Danckaert, and I. Fischer, "Constructing optimized binary masks for reservoir computing with delay systems," *Sci Rep*, vol. 4, no. 1, Art. no. 1, Jan. 2014, doi: 10.1038/srep03629.

[29] T. Hiraki *et al.*, "Membrane InGaAsP Mach–Zehnder Modulator Integrated With Optical Amplifier on Si Platform," *J. Lightwave Technol., JLT*, vol. 38, no. 11, pp. 3030–3036, Jun. 2020, doi: 10.1364/JLT.38.003030.

[30] T. Aihara *et al.*, "Mach-Zehnder Modulator using Membrane InGaAsP Phase Shifters and SOAs inside Interferometer Arms on Si Photonics Platform," in *Optical Fiber Communication Conference (OFC) 2020 (2020), paper M2B.5*, Optica Publishing Group, Mar. 2020, p. M2B.5. doi: 10.1364/OFC.2020.M2B.5.

[31] J. Dambre, D. Verstraeten, B. Schrauwen, and S. Massar, "Information Processing Capacity of Dynamical Systems," *Sci Rep*, vol. 2, no. 1, p. 514, Jul. 2012, doi: 10.1038/srep00514.

[32] T. Hiraki, T. Aihara, H. Nishi, and T. Tsuchizawa, "Deuterated SiN/SiON Waveguides on Si Platform and Their Application to C-Band WDM Filters," *IEEE Photonics Journal*, vol. 9, no. 5, pp. 1–7, Oct. 2017, doi: 10.1109/JPHOT.2017.2731996.

[33] T. Aihara *et al.*, "Membrane buried-heterostructure DFB laser with an optically coupled III-V/Si waveguide," *Opt. Express, OE*, vol. 27, no. 25, pp. 36438–36448, Dec. 2019, doi: 10.1364/OE.27.036438.

[34] K. Takeda *et al.*, "Optical links on silicon photonic chips using ultralow-power consumption photonic-crystal lasers," *Optics Express*, vol. 29, no. 16, pp. 26082–26092, 2021.

Takuma Tsurugaya was born in Gunma, Japan, in 1992. He received the B.E. and M.E. degrees in electrical and electronic engineering from the University of Tokyo, Tokyo, Japan, in 2016 and 2018, respectively.

In 2018, He joined NTT Device Technology Laboratories, Atsugi, Japan. His research interests include development of photonic-crystal nanolasers and application of semiconductor optical devices for photonic neural networks.

Mr. Tsurugaya is a Member of the Japan Society of Applied Physics (JSAP) and Institute of Electronics, Information and Communication Engineers (IEICE). He was the recipient of the Young Scientist Presentation Award from the JSAP in 2021 and the Young Researcher's Award from the IEICE in 2022.

Tatsurou Hiraki (Member, IEEE) received the B.E., M.E., and Ph.D. degrees from Tohoku University, Sendai, Japan, in 2009, 2011, and 2017, respectively.

In 2011, he joined NTT Microsystem Integration Laboratories, Nippon Telegraph and Telephone Corporation, Kanagawa, Japan. His research interests include heterogeneously integrated III-V semiconductor optical modulators, optical amplifiers, and laser diodes on Si photonics circuits.

Dr. Hiraki is a Member of the Institute of Electronics, Information and Communication Engineers (IEICE) and Japan Society of Applied Physics (JSAP).

Takuma Aihara (Associate Member, IEEE) was born in Akita, Japan, in 1987. He received the B.E., M.E., and Ph.D. degrees in electrical and electronic information engineering from the Toyohashi University of Technology, Toyohashi, Japan, in 2010, 2012, and 2015, respectively.

In 2015, he joined NTT Device Technology Laboratories. He has been researching the III-V semiconductor lasers on Si photonic integrated circuits.

Dr. Aihara is a Member of the Japan Society of Applied Physics (JSAP).

Mitsumasa Nakajima (Member, IEEE) received the M.E. and Ph.D. degrees in material science from the Tokyo Institute of Technology, Tokyo, Japan, in 2010 and 2015, respectively.

In 2010, he joined the Nippon Telegraph and Telephone (NTT) Laboratories, Atsugi, Japan, where he was involved in the development of large-scale optical switches. His research interests are optical devices and their applications including neuromorphic photonics and optical signal processing for telecom.

Dr. Nakajima is a member of the Institute of Electronics, Information and Communication Engineers (IEICE) and The Japan Society of Applied Physics (JSAP). He was a recipient of the Young Engineer Award from the IEICE of Japan.

Nikolaos-Panteleimon Diamantopoulos (Senior Member, IEEE) was born in Athens, Greece, in 1988. He received the B.Sc. degree from the University of Peloponnese, Tripoli, Greece, in 2009, the two M.Sc. degrees from Aston University, Birmingham, U.K., and Scuola Superiore Sant'Anna, Pisa, Italy, in 2012, under the joint-master's Erasmus Mundus Program, and the Ph.D. degree from Osaka University, Suita, Japan, in 2016.

Between 2011 and 2016, he was involved in several EU-funded R&D projects with the Athens Information Technology Research Center, Greece. Since 2016, he has been with NTT Device Technology Laboratories, Atsugi, Japan. His research interests include integrated photonics, optical communications, signal processing, and semiconductor lasers.

Dr. Diamantopoulos is a Senior Member of IEEE and OPTICA.

Toru Segawa (Member, IEEE) received the B.E. and M.E. degrees in electrical engineering and the Ph.D. degree in integrated design engineering from Keio University, Yokohama, Japan, in 1999, 2001, and 2012, respectively.

In 2001, he joined NTT Photonics Laboratories, Atsugi, Japan, and has been engaged in research on high-speed tunable lasers and optical switches monolithically integrated on InP substrates. He is currently with the NTT Device Technology Laboratories, Atsugi, Japan.

Dr. Segawa is a Member of the JSAP and IEICE.

Shinji Matsuo (Fellow, IEEE) received the B.E. and M.E. degrees in electrical engineering from Hiroshima University, Hiroshima, Japan, in 1986 and 1988, respectively, and the Ph.D. degree in electronics and applied physics from the Tokyo Institute of Technology, Tokyo, Japan, in 2008.

In 1988, he joined NTT Optoelectronics Laboratories, where he researched photonic functional devices using multiple quantum well pin modulators and VCSELs. In 1997, he researched optical networks using WDM technologies with NTT Network Innovation Laboratories. Since 2000, he has been researching lasers and heterogeneous integration of III-V and Si photonics devices at NTT Photonics Laboratories, Atsugi, Japan and NTT Device Technology Laboratories, Atsugi, Japan.

Dr. Matsuo is a Fellow of NTT. He is a Member of the JSAP and IEICE, and a Fellow of OPTICA.

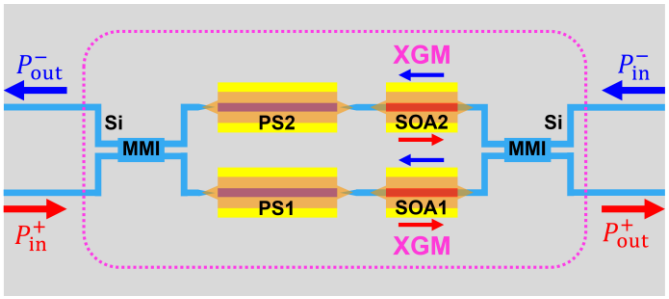

Fig. 1. Device configuration of the SOA-MZI and its XGM-based computing functionality as a two-input two-output nonlinear processor.

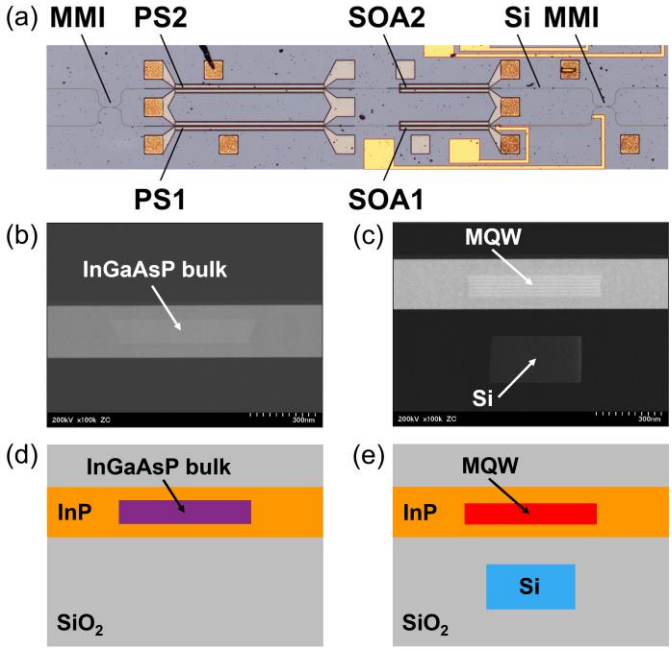

Fig. 2. (a) Optical microscope image of the SOA-MZI. (b),(c) Cross-sectional SEM images of the membrane PS and SOA, respectively. (d),(e) Corresponding cross-sectional schematics of the membrane PS and SOA, respectively.

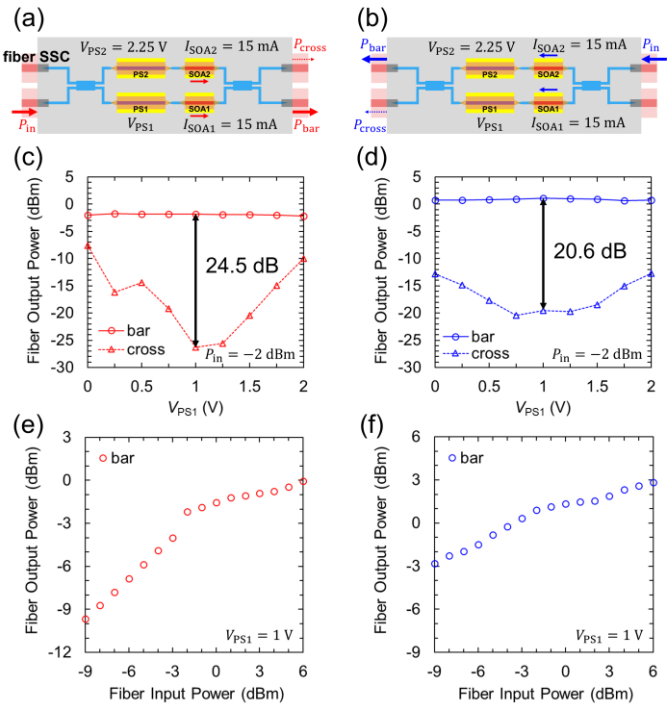

Fig. 3. (a),(b) Contrast ratio measurement setups for forward and backward directions, respectively. (c),(d) Fiber output powers at the bar and cross ports measured as a function of V_{PS1} with P_{in} set to -2 dBm for the setups of (a) and (b), respectively. (e),(f) Fiber output powers at the bar ports measured as a function of P_{in} with V_{PS1} set to 1 V for the setups of (a) and (b), respectively.

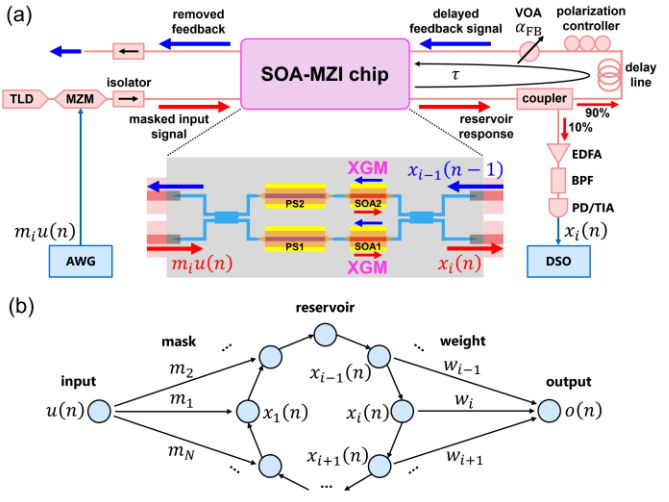

Fig. 4. (a) Schematic of the XGM-based RC system implemented using the SOA-MZI chip and a fiber delay line. (b) Its equivalent network structure.

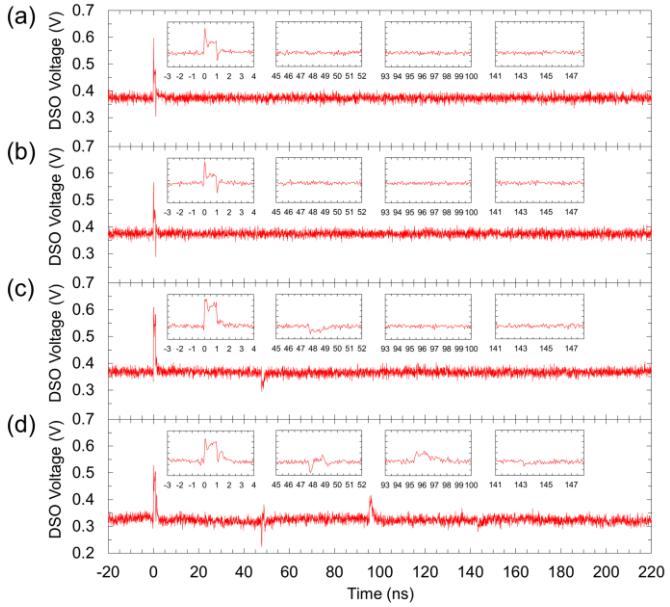

Fig. 5. Impulse responses of the RC system measured under the feedback attenuations of (a) full cutoff, (b) 10 dB, (c) 4 dB, and (d) 2 dB.

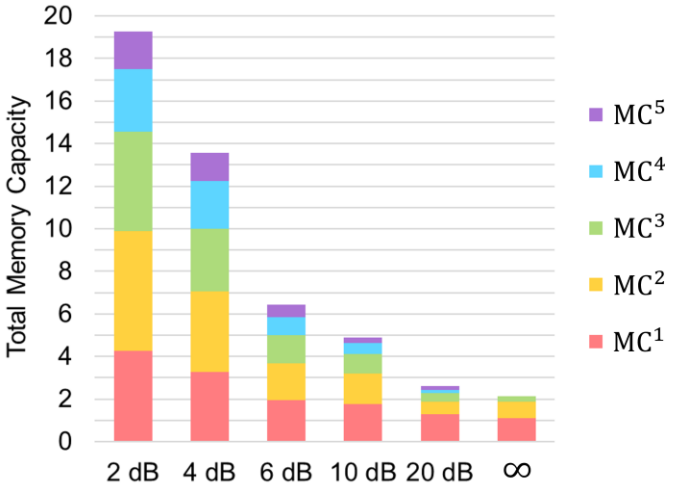

Fig. 7. Information processing capacity (IPC) for each feedback attenuation whose TMC is highest among the three-time measurements.

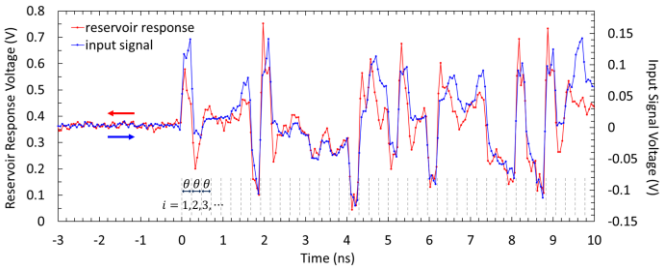

Fig. 6. Example of experimental data measured for the RC performance evaluation. The feedback attenuation was set to 2 dB. The gray dashed lines indicate the time slots of virtual nodes with each interval of θ.

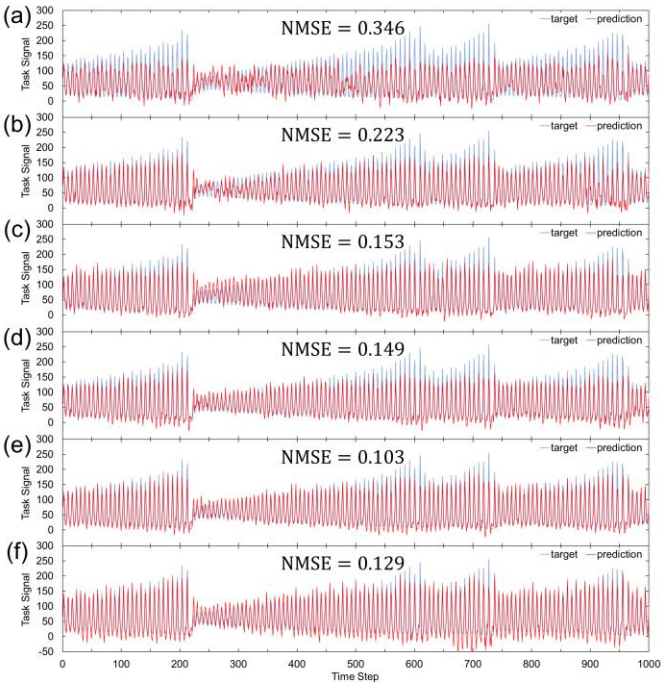

Fig. 8. Testing results for the Santa-Fe times-series prediction task under the feedback attenuations of (a) full cutoff, (b) 20 dB, (c) 10 dB, (d) 6 dB, (e) 4 dB, and (f) 2 dB. Each shows the result whose NMSE is lowest among the three-time measurements. The NMSE value is shown in each graph.

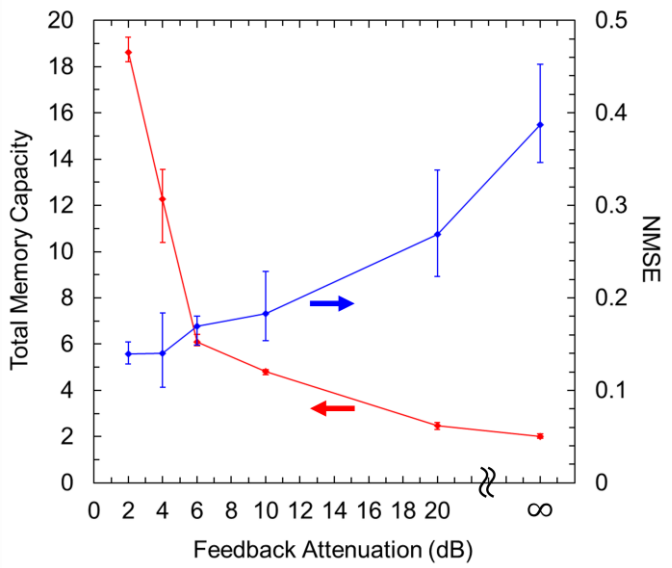

Fig. 9. TMC and NMSE values averaged over the three data points for each feedback attenuation. Each error bar indicates the maximum and minimum values among the three.

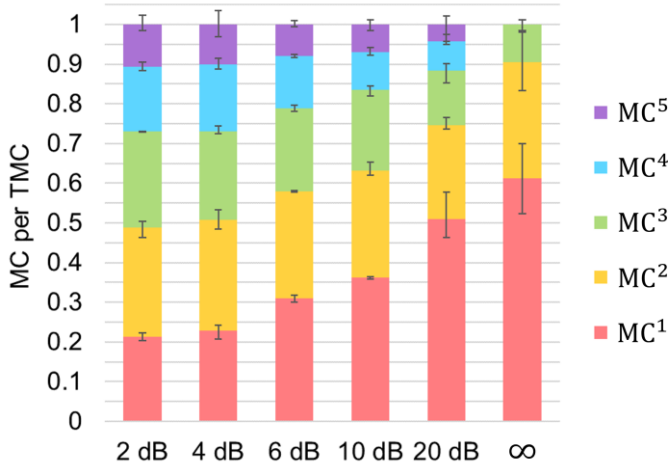

Fig. 10. Normalized MCs averaged over the three data points for each polynomial degree *D* and each feedback attenuation. Each error bar indicates the maximum and minimum normalized MCs among the three.